Shape evolution of numerically obtained subaqueous barchan dunes

Carlos A. Alvarez ⬡* and Erick M. Franklin ⬡†
School of Mechanical Engineering, UNICAMP–University of Campinas,
Rua Mendeleyev, 200, Campinas, SP, Brazil

In the realm of granular bedforms, barchan dunes are strong attractors that can be found in rivers, terrestrial deserts, and other planetary environments. These bedforms are characterized by a crescentic shape, which, although robust, presents different scales according to the environment they are in, their length scale varying from the decimeter under water to the kilometer on Mars. In addition to the scales of bedforms, the transport of grains presents significant differences according to the nature of the entraining fluid, so that the growth of barchans is still not fully understood. Given the smaller length and time scales of the aquatic case, subaqueous barchans are the ideal object to study the growth of barchan dunes. In the present paper, we reproduce numerically the experiments of Alvarez and Franklin [Phys. Rev. E **96**, 062906 (2017); Phys. Rev. Lett. **121**, 164503 (2018)] on the shape evolution of barchans from their initiation until they have reached a stable shape. We computed the bed evolution by using the computational fluid dynamics–discrete element method, where we coupled the discrete element method with large eddy simulation for the same initial and boundary conditions of experiments, performed in a closed-conduit channel where initially conical heaps evolved to single barchans under the action of a water flow in a turbulent regime. Our simulations captured well the evolution of the initial pile toward a barchan dune in both the bedform and grain scales, with the same characteristic time and lengths observed in experiments. In addition, we obtained the local granular flux and the resultant force acting on each grain, the latter not yet previously measured nor computed. This shows that the present method is appropriate for numerical computations of bedforms, opening new possibilities for accessing data that are not available from current experiments.

I. INTRODUCTION

Under the action of a fluid flow, granular beds may give rise to ripples and dunes. Among the different bedforms, barchan dunes are strong attractors that can be found in highly diverse environments such as rivers, oil pipelines, open channels, terrestrial deserts, and even other planetary environments [1–4]. Barchans are usually formed when grains are transported as bed load by a one-directional fluid flow, and they are characterized by a crescentic shape with horns pointing downstream [1,2]. Although robust, this shape presents different scales according to the environment the barchans are in, varying from the decimeter and minute under water [5,6] to the kilometer and millennium on Mars [3,4].

Besides the bedform scales, the transport of grains is different according to the nature of the entraining fluid. In liquids, bed load is characterized by grains that move by rolling and sliding over each other [7], and occasionally by small jumps with distances of the order of a few grain diameters [8,9], while in gases bed load is characterized by ballistic flights over distances much larger than the grain diameter [1,8]. Because of shape and transport differences, a general explanation for the growth of barchans is still lacking.

Given the smaller length and time scales of the aquatic case, subaqueous barchans are the ideal object to study the growth of barchan dunes. For this reason, many studies carried out experiments in water tanks and channels in order to obtain the length and time scales of barchans [2,6,10–12] and typical trajectories and velocities of moving grains [13–15]. The smaller and faster scales of the subaqueous case have allowed the establishment of relations and scaling factors crucial to understand the dynamics of much larger and slower barchans found in other environments [2–4].

Another way to investigate the dynamics of barchans is by carrying out numerical simulations. The first numerical works computing large-scale dunes employed continuum models for the grains [16–22] and considered that saltation was the mode of entrainment, occurring mainly in the longitudinal direction, with some transverse diffusion. Therefore, those models are suitable to simulations of Aeolian and Martian dunes consisting of a large number of salting grains, in which, indeed, they succeeded. However, the transverse displacements of grains in the subaqueous case are, on average, comparable to the longitudinal ones, as shown recently by Refs. [13–15], a situation different from what is generally conjectured for the Aeolian and Martian cases. If we consider that subaqueous barchans measure a few decimeters, consisting of only some tens of thousands of grains, and that saltation is not the preferable mode of entrainment, then continuous models are not well justified in the aquatic case, although they may give reasonable results if the transverse diffusion is tuned

---

*calvarez@fem.unicamp.br
†Author to whom all correspondence should be addressed: franklin@fem.unicamp.br

appropriately or if bed load is considered to follow more closely the fluid. For example, Khosronejad and Sotiropoulos [23] succeeded in computing fields of subaqueous barchans by using a continuum model for the grains. They coupled a large eddy simulation (LES) model for the water and water-suspension mixture with a continuum model involving the entrainment and Exner equations for the granular bed, obtaining morphological characteristics of bedforms during the evolution of an initially flat bed toward a barchan field. However, the dynamics at the grain scale is not accessible with this method.

More recently, simulations of bed load as a discrete medium by using Euler-Lagrange methods, such as the computational fluid dynamics–discrete element method (CFD-DEM), succeeded in capturing the main features of bed load [24–28] and bedforms [29,30]. Schmeeckle [24] presented a model coupling DEM with LES based on the open source codes CFDEM [31] (www.cfdem.com), OPENFOAM (www.openfoam.org), and LIGGGHTS [32,33], that was used to compute sand transport by water. The author carried out computations for different flow strengths over initially flat beds, being interested essentially in the entrainment of grains by the water flow. His results showed that bed-load grains move generally in contact with the bed and that saltation is of lesser importance in the subaqueous case, with most of the grains being dislodged directly by the water flow. Pähtz and Durán [28] investigated numerically the mechanisms of the entrainment of grains by using DEM coupled with Reynolds-averaged Navier-Stokes equations (RANS). The authors examined the conditions for entrainment directly by the fluid (fluid entrainment) and particle-bed impacts (impact entrainment), and they found that fluid entrainment is important only for viscous cases, the impact entrainment being more important in all the other cases. For a given range of flows, Refs. [24] and [28] present contrasting results with respect to grain entrainment.

Kidanemariam and Uhlmann [25,29,30] numerically investigated bed load and the growth of bedforms in the subaqueous case. The authors used direct numerical simulations (DNS) for the fluid, DEM for the grains, and immersed boundary (IB) for the coupling between fluid and grains. Their simulations showed that bed load is computed properly by the proposed method, and wavelengths, amplitudes, and celerities of bedforms are well captured, being in agreement with experimental data available in the literature. The proposed methodology is currently the most accurate, avoiding the use of turbulence models for the fluid, capturing all the scales of turbulence down to the Kolmogorov scale, and fully solving the flow around each grain. However, the computational cost is exceedingly high, so that the time required for obtaining developed bedforms is seldom reached [34].

Although some numerical investigations succeeded in capturing the formation of subaqueous barchans, they did not report detailed measurements in the bedform and grain scales, namely the evolution of lengths and times of bedforms and the trajectories of individual grains over barchans. In addition, the role of water in the direct entrainment of grains is still a subject of debate. Detailed morphological evolution, local characteristics of the water flow, and trajectories of individual grains obtained from numerical computations are important to evaluate the suitability of numerical methods and pro-

vide information not accessible from reported experiments, such as the mode of entrainment and resultant forces on grains.

A. Prior work

In previous studies [12,13], we investigated experimentally the morphology and the trajectories of grains migrating to horns during the growth of subaqueous barchans. The experiments were conducted in a closed-conduit channel where initially conical heaps evolved to single barchans under the action of a turbulent water flow. The bedforms consisted of glass beads with diameters within $0.15 \leqslant d \leqslant 0.25$ mm and $0.40 \leqslant d \leqslant 0.60$ mm, and the cross-sectional mean velocities of water U were 0.243, 0.294, and 0.364 m/s, corresponding to shear velocities on the bottom wall of the channel u_* of 0.0141, 0.0168, and 0.0202 m/s, respectively. Based on the experimental results, we found the characteristic times $0.5t_c$ and $2.5t_c$ for the growth and equilibrium of barchans, respectively, where t_c is a proposed time scale computed as the length of the bedform divided by its celerity, and we found that most of the grains migrating to horns during the growth of barchans were initially on upstream regions at the periphery of the initial pile, the grains traveling with significant transverse displacements.

B. This study

In this paper, we reproduce numerically some of the experimental results of Alvarez and Franklin [12,13] on the shape evolution of barchans, from their initiation until they have reached a stable shape, and the trajectories of grains migrating to horns. Besides the evolution of the bedform morphology and the trajectory of grains, we obtained numerically the local granular flux and the resultant force acting on each grain, for which data are still missing in the literature, and the local water flow over a single barchan, which we compare with the experiments of Charru and Franklin [35]. Our simulations were performed by using CFD-DEM to compute numerically the formation of single barchans from initially conical piles, where the fluid was computed with LES and the grains by solving linear and angular momentum equations applied to each particle. LES, although needing subgrid turbulence models, is able to compute the flow around bedforms including recirculation regions and some large turbulence structures, with a much lower computational cost than DNS. Our simulations captured well not only the formation of barchans, but also their length scale, the time scale t_c for the growth of horns, the trajectories of grains migrating to horns, the local flux of grains, and the resultant force acting on each grain. Our results show that the used method is appropriate to numerical computations of subaqueous bedforms, opening new possibilities for accessing data not available from current experiments.

In the following, Secs. II and III present, respectively, the model equations and numerical setup, and Sec. IV presents the results for the bedform morphology, local characteristics of the water flow over developed barchans, trajectory of individual grains, local flux of grains, and resultant force acting on each grain. Section V presents the conclusions.

II. MODEL DESCRIPTION

Our numerical investigation was conducted with CFD-DEM, where the dynamics of each individual particle was computed by DEM [36] using the resulting forces and torques on each particle, the fluid flow was computed by LES, and momentum coupling was made between solids and fluid.

A. Grains

The solid particles are treated in a Lagrangian framework, with the dynamics of each particle being computed by the linear and angular momentum equations, given by Eqs. (1) and (2), respectively,

$$m_p \frac{d\vec{u}_p}{dt} = \vec{F}_{fp} + \vec{F}_c + m_p \vec{g}, \tag{1}$$

$$I_p \frac{d\vec{\omega}_p}{dt} = \vec{T}_c, \tag{2}$$

where $\vec{g}$ is the acceleration of gravity and, for each particle, m_p is the mass, $\vec{u}_p$ is the velocity, I_p is the moment of inertia, $\vec{\omega}_p$ is the angular velocity, $\vec{F}_{fp}$ is the resultant of fluid forces on grains, $\vec{F}_c$ is the resultant of contact forces between solids, and $\vec{T}_c$ is the resultant of contact torques between solids. In the balance of angular momentum, Eq. (2), we neglect momentum variations caused by the fluid because the term due to contacts is much higher [26,37,38]. In the present study, we consider that the resultant of fluid forces acting on each particle is made up of components given by the fluid drag, fluid stresses, and added mass:

$$\vec{F}_{fp} = \vec{F}_D + \vec{F}_{\text{stress}} + \vec{F}_{\text{am}}, \tag{3}$$

where $\vec{F}_D$ is the drag force caused by the fluid on grains, $\vec{F}_{\text{stress}} = V_p[-\nabla P + \nabla \cdot \vec{\vec{\tau}}]$ is the force caused by fluid stresses, and $\vec{F}_{\text{am}}$ is the added mass force, V_p being the volume of one solid particle, P the fluid pressure, and $\vec{\vec{\tau}}$ the deviatoric stress tensor of the fluid. In Eq. (3), we neglect the Basset, Saffman, and Magnus forces as they are usually considered of lesser importance in CFD-DEM simulations [39].

The contact forces and torques are the result of contacts between particles and between particles and the wall. They can be expressed, respectively, by Eqs. (4) and (5),

$$\vec{F}_c = \sum_{i \neq j}^{N_c} (\vec{F}_{c,ij}) + \sum_{i}^{N_w} (\vec{F}_{c,iw}), \tag{4}$$

$$\vec{T}_c = \sum_{i \neq j}^{N_c} \vec{T}_{c,ij} + \sum_{i}^{N_w} \vec{T}_{c,iw}, \tag{5}$$

where $\vec{F}_{c,ij}$ and $\vec{F}_{c,iw}$ are the contact forces between particles and between particles and the wall, respectively, $\vec{T}_{c,ij}$ is the torque due to the tangential component of the contact force between particles i and j, and $\vec{T}_{c,iw}$ is the torque due to the tangential component of the contact force between particle i and the wall, $N_c - 1$ being the number of particles in contact with particle i, and N_w the number of particles in contact with the wall.

TABLE I. DEM parameters.

Particle diameter d (mm)	0.5
Particle density ρ_p (kg/m^3)	2500
Young's modulus E (MPa)	5
Poisson ratio σ	0.45
Restitution coefficient e	0.1
Friction coefficient μ_{fr}	0.6
Initial number of particles N	4×10^4
Time step (s)	5×10^{-6}

B. Fluid

The fluid is the continuous phase and is treated in an Eulerian framework. For an incompressible flow, mass and momentum equations are given by Eqs. (6) and (7), respectively,

$$\nabla \cdot \vec{u}_f = \mathbf{0}, \tag{6}$$

$$\frac{\partial \rho_f \vec{u}_f}{\partial t} + \nabla \cdot (\rho_f \vec{u}_f \vec{u}_f) = -\nabla P + \nabla \cdot \vec{\vec{\tau}} + \rho_f \vec{g} - \vec{f}_{fp}, \tag{7}$$

where $\vec{u}_f$ is the fluid velocity, ρ_f is the fluid density (equal to 10^3 kg/m^3 in the present case), and $\vec{f}_{fp}$ is the resultant of fluid forces acting on each grain, $\vec{F}_{fp}$, by unit of fluid volume, representing the momentum transfer from the fluid to the solids.

III. NUMERICAL SETUP

In the present study, we used the open source code CFDEM [31] (www.cfdem.com) for our CFD-DEM computations. CFDEM links the open source code OPENFOAM, which computes the fluid flow based on the finite volume method (FVM), with the open source code LIGGGHTS [32,33], which computes the dynamics of grains.

Concerning the grains, we considered a Hertzian model for which we set up the coefficient of restitution e as approximately 0.1 because collisions are expected to be viscous damped [24]. The friction coefficient μ_{fr} was considered as 0.6 [24,26], and Young's modulus E and the Poisson ratio σ were obtained from Refs. [37,38]. Young's modulus used in the simulations is considerably smaller than real values in order to reduce the DEM time step without affecting significantly the numerical outputs [38]. The main parameters used in our simulations are listed in Table I.

For the fluid, we used LES with subgrid stresses given by the wall-adapting local eddy-viscosity (WALE) model [40]. The domain was set to $0.3 \times 0.05 \times 0.16$ m divided into 150, 150, and 160 segments in the streamwise, x, wall-normal, y, and spanwise, z, directions, respectively. The dimensions in $y = 2\delta$ and z directions are the same as those of previous experiments [12,13,15]. The segments in the x and z directions are uniform in size, whereas in the y direction they are unevenly spaced. Details of the grid and Reynolds numbers employed in our simulations are summarized in Table II, where $\text{Re} = U 2\delta \nu^{-1}$ is the channel Reynolds number based on the cross-sectional mean velocity and $\text{Re}_* = u_* \delta \nu^{-1}$ is the Reynolds number based on the shear velocity, ν being the kinematic viscosity (equal to 10^{-6} m^2/s in the present case).

TABLE II. Computational grid and Reynolds numbers. Δx^+ and Δz^+ are the grid spacings Δx and Δz in the streamwise and spanwise directions, respectively, scaled in inner wall units, νu_*^{-1}. Δy_1^+ and Δy_c^+ are the grid spacing in the wall-normal direction at the first and center points, respectively, scaled in inner wall units. $\mathrm{Re} = U 2\delta \nu^{-1}$ and $\mathrm{Re}_* = u_* \delta \nu^{-1}$, where U is the cross-sectional mean velocity.

	Case 1	Case 2
Δx^+	33.6	40.4
Δy_1^+	0.91	1.10
Δy_c^+	17.18	20.65
Δz^+	16.80	20.20
Re	1.47×10^4	1.82×10^4
Re_*	420	506

In Eq. (7), the term of momentum transfer between the fluid and solids is computed as $\vec{f}_{fp} = \vec{F}_{fp}/V_{\mathrm{cell}}$, where V_{cell} is the volume of the considered computational cell. The drag force in Eq. (3) is computed as in Eq. (8),

$$\vec{F}_D = A_p C_D \rho_f (\vec{u}_f - \vec{u}_p)|\vec{u}_f - \vec{u}_p|, \tag{8}$$

where A_p is the particle cross-sectional area and C_D is a drag coefficient obtained from the Gidaspow model [41].

Prior to CFD-DEM simulations, single phase flows were computed in the computational domain, corresponding to a rectangular cross-sectional channel. Periodic conditions were considered in streamwise and spanwise directions, and the final realization was saved to be used as the fluid initial condition for the CFD-DEM simulations with grains.

Also prior to starting the simulations, the water flow was set to zero velocity and the grains were poured from above, falling freely in water at a longitudinal location 0.05 m from the domain inlet and centered in the transverse direction. After a period for the grains to settle, we obtained an initially conical pile with radius $R = 0.025$ m, similar to Refs. [12,13,15], and center at 0.05 m from the domain inlet. Once the initial condition for the grains was reached, we imposed the final realization of the single-phase LES computations as the initial condition for water. The boundary conditions for the fluid were impermeability and no-slip conditions at the top and bottom walls of the channel, and periodic conditions in the longitudinal and transverse directions. The boundary conditions for the solid particles were solid walls at the top and bottom walls, free exit at the outlet, and no mass entering at the inlet, so that the barchan decreased slightly in size while migrating, in the same manner as in Refs. [12,13,15]. Figure 1 shows a layout of the computational domain.

The resulting conditions for sediment transport are $s = 2.5$, Ga $= 43$, Im $= 74$, and $\theta = 0.04$ and 0.06, where $s = \rho_p/\rho_f$ is the density ratio, Ga $= \sqrt{(s-1)gd^3}/\nu$ is the Galileo number, $\theta = u_*^2/[(s-1)gd]$ is the Shields number, and Im $=$ Ga$\sqrt{s+0.5}$ is the impact number proposed by Pähtz and Durán [28] to account for the importance of impact entrainment on bed load and saltation. In the present case, $3 \leqslant \theta \times$ Im $\leqslant 4$ and Im > 20, placing the bed-load conditions in the limit between fluid and impact entrainment, according to Ref. [28]. The experiments reported in Refs. [12,13,15] showed grains rolling and sliding following closely the mean
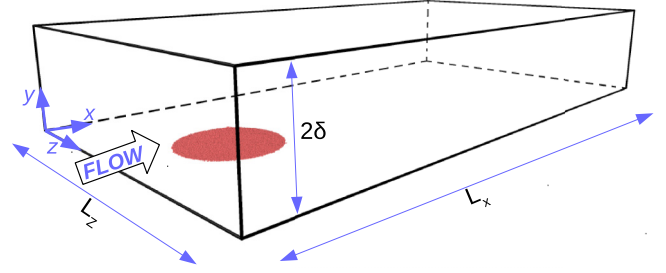

FIG. 1. Layout of the computational setup. In the simulations, $L_x = 0.3$ m, $2\delta = 0.05$ m, and $L_z = 0.16$ m.

water flow, pointing in the direction of direct entrainment by the fluid.

The tracking of bedforms and individual grains, as well as computations of morphology characteristics and grain trajectories, were carried out in the same manner as in our previous experiments [12,13,15], making use of scripts written for this purpose based on Refs. [42,43].

IV. RESULTS AND DISCUSSION

A. Single water flow

Computations of single-phase channel flows were necessary to be used as the initial condition for the simulations with solid particles. To evaluate our LES computations, the single phase simulations for $\mathrm{Re}_* = 420$ were compared with the DNS results of Moser *et al.* [44] for $\mathrm{Re}_* = 395$. For that, we averaged 1000 velocity fields in time (the last of 3000 fields) and in the x and z directions, obtaining the profiles of mean velocity and Reynolds stress, which were compared afterward with Ref. [44].

Figures 2(a) and 2(b) present, respectively, the profiles of the longitudinal component of the mean velocity in the traditional log-normal scales and of the components of the Reynolds stress, normalized by the inner scales, where solid lines correspond to the present LES results and dashed lines to the DNS results of Moser *et al.* [44]. In these figures, u is the longitudinal component of the mean velocity, $u^+ = u/u_*$, k is the turbulent kinetic energy, and u', v', and w' are the longitudinal, vertical, and transverse components of velocity fluctuations, respectively. In the case of velocity fluctuations and turbulent kinetic energy, the superscript $+$ means division by u_*^2, an overbar means temporal averages, and $\langle \rangle$ refers to spatial averages in the x and z directions. Figure 2(a) presents also the law of the wall with $\kappa = 0.41$ and $B = 5.2$.

In Fig. 2(a) we can observe that in the viscous region, the mean profile obtained with LES shows a good agreement with both the law of the wall and DNS results of Ref. [44], while in the overlap region LES results are shifted upward with the same slope when compared with both the law of the wall and DNS. LES results could have a better agreement with DNS if we further refined the mesh; however, we are not carrying out particle-resolved simulations, so that the present results are adequate for the purpose of initial conditions for simulations with bed load. Figure 2(b) shows a good agreement between second-order moments obtained by LES and DNS. Finally, we observe that two-dimensional measurements with particle
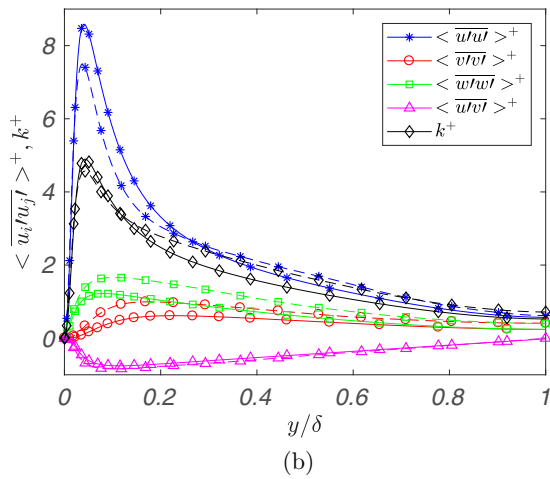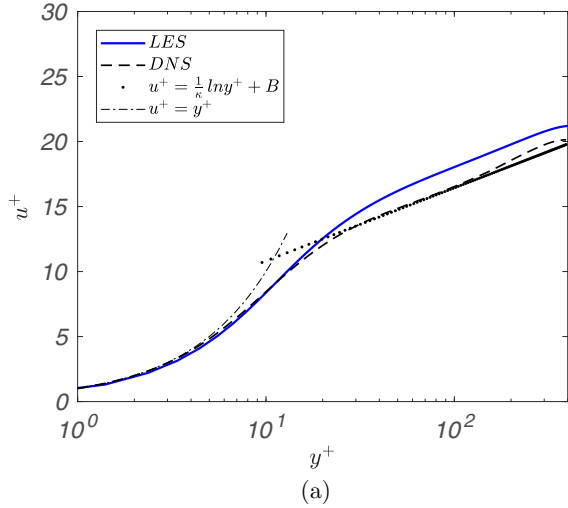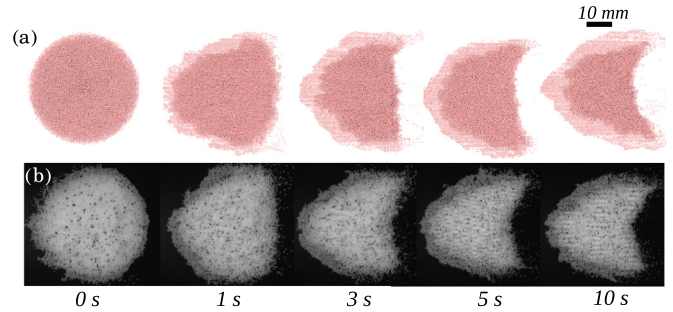
(a)

10 mm

(b)

0 s   1 s   3 s   5 s   10 s

FIG. 3. Top views of an initially conical heap deformed by a turbulent water flow at different times. The flow is from left to right. (a) Numerical results. (b) Experiments of Ref. [13]. Re $= 1.82 \times 10^4$, $d = 0.5$ mm, and $\rho_p = 2500$ kg/m^3.

Figure 3(b) corresponds to images from experiments for Re $= 1.82 \times 10^4$, $d = 0.5$ mm, and $\rho_p = 2500$ kg/m^3, and Fig. 3(a) consists of snapshots of our numerical simulations for the same conditions. From the snapshots and Refs. [13,47], we observe a similar evolution of bedforms in experiments and
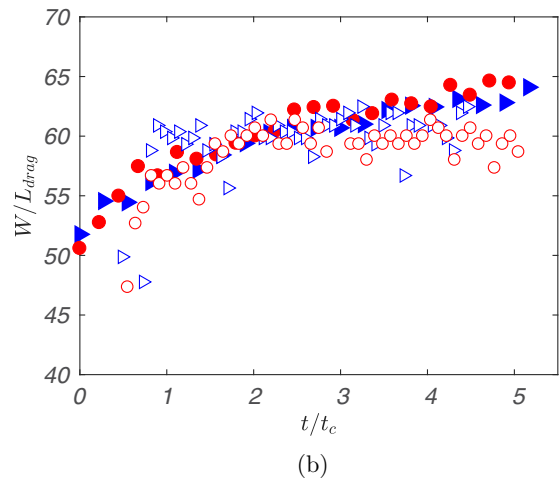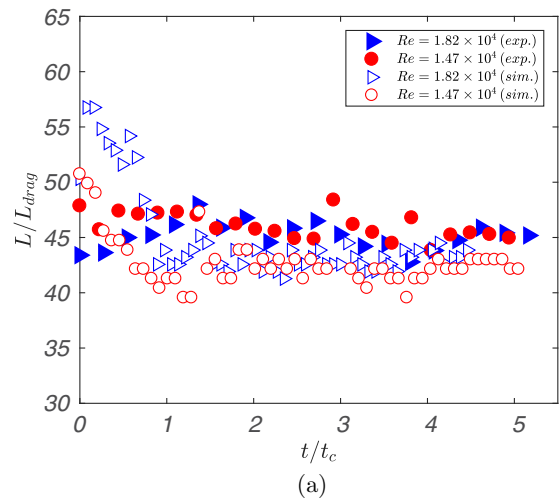

FIG. 2. Single-phase flow in the channel. (a) Profile of the longitudinal component of the mean velocity u in the traditional log-normal scales, normalized by the inner scales. (b) Profiles of the components of the Reynolds stress and turbulent kinetic energy normalized by the inner scales. Solid lines correspond to the present LES results (for Re$_* = 420$) and dashed lines to the DNS results of Moser *et al.* [44] (for Re$_* = 395$). Part (a) presents also the law of the wall with $\kappa = 0.41$ and $B = 5.2$.

image velocimetry (PIV) in a channel with the same dimensions provided similar results [45,46].

B. Simulations with bed load

1. Morphology of bedforms

With the grains settled in the channel, forming an initially conical pile, the output of the LES simulation for the single-phase flow was imposed as the initial condition for the fluid. Once the simulations started, with periodic conditions for the fluid in the x and z directions, the turbulent flow was sustained and the grains entrained by the water flow, deforming the initial pile in a barchan dune, as can be seen in Fig. 3 and in a movie from one numerical simulation available in the Supplemental Material [47].

Figure 3 shows top views of the bedform as it is deformed from a conical heap in a barchan dune by the water flow.

FIG. 4. (a) L/L_{drag} vs t/t_c and (b) W/L_{drag} vs t/t_c. The open symbols correspond to numerical results, solid symbols to the experimental results of Refs. [12,13], and Reynolds numbers are listed in the key.
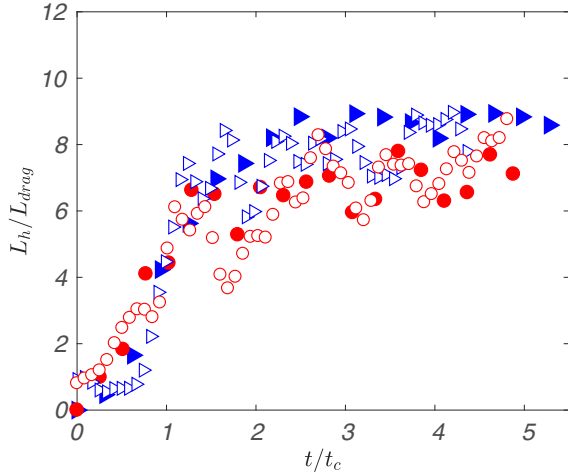
FIG. 5. L_h/L_{drag} vs t/t_c. The open symbols correspond to numerical results, solid symbols to the experimental results of Refs. [12,13], and Reynolds numbers are listed in the key of Fig. 4(a).
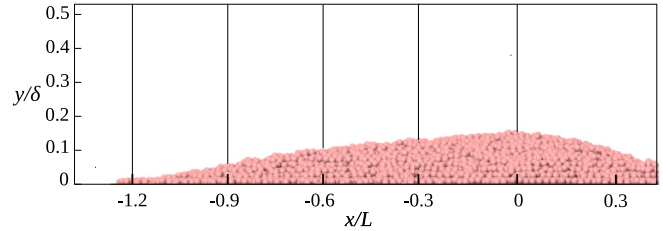

FIG. 6. Side view of a barchan dune, showing the adopted coordinate system for the flow over the dune. Vertical lines correspond to the longitudinal positions of the profiles plotted in Figs. 7 and 8.

numerical simulations: once the water starts to flow, the pile is deformed, with the formation of a slip face and growing of horns. After some time, the bedform adopts a crescentic shape. The evolution of length and time scales is discussed next.

A direct comparison between experiments and numerical simulations for the evolutions of the length and width of barchans is presented in Fig. 4. Figures 4(a) and 4(b) show, respectively, the length L and width W of barchans normalized by the length scale L_{drag} as functions of time t normalized by the timescale t_c. The open symbols correspond to numerical results, solid symbols to the experimental results of Refs. [12,13], and Reynolds numbers are listed in the key of Fig. 4(a). $L_{\mathrm{drag}} = (\rho_s/\rho_f)d$ is an inertial length for the Aeolian case [2,16], which is proportional to the length for the stabilization of sand flux, and $t_c = L_{\mathrm{eq}}/C$ is the time scale for the barchan evolution [12], where L_{eq} is the barchan length once the crescentic shape is attained and C is the dune celerity.

For $t < t_c$, the numerically obtained values are different from the experimental ones, with, in addition, a different behavior for L, which decreases in the numerical results while it remains constant in the experiments. The difference in the initial behavior is due to slight differences in the initial conditions of numerical simulations when compared to experiments. In their turn, part of the differences in the initial conditions results from the pouring of grains on the bottom wall, where the friction coefficient between grains and wall is fixed in the numerical simulations, but is susceptible to variations and uncertainties in the experiments. In general, the bedforms in numerical simulations and experiments evolve in a similar manner, reaching roughly the same length and width for $t \geqslant t_c$.

The time evolution of the length of horns L_h is shown in Fig. 5, which presents L_h/L_{drag} as a function of t/t_c. The open symbols correspond to numerical results, solid symbols to the experimental results of Refs. [12,13], and Reynolds numbers are listed in the key of Fig. 4(a). In the case of L_h, the numerical results show a good agreement with experiments,

the length increasing with the same slope for $t < 2.5t_c$ and reaching the same constant value for $t \geqslant 2.5t_c$.

Arguing that the main feature of a barchan dune is its horns, Alvarez and Franklin [12] proposed, based on the evolution of horns, that an initially conical pile deforms under the action of a water flow and reaches a stable crescentic shape when $t = 2.5t_c$. For $t \geqslant 2.5t_c$, the subaqueous barchan migrates keeping the same crescentic shape, being referred to in Ref. [12] as stable dunes. Because our numerical simulations predict the same evolution for horns at all times, and similar behaviors for the dune length and width for $t \geqslant t_c$, we consider that the present simulations capture well the morphology of evolving barchans.

2. Flow over single barchans

Second-order moments for the flow over a barchan dune were obtained by time averaging 10 000 instantaneous fields (the last of 20 000 fields) in the vertical symmetry plane of the dune. Because the flow evolves along the dune, we present next only some profiles along the stoss side until reaching the dune crest. To obtain a significant number of fields while allowing a direct comparison with the PIV experiments reported in Charru and Franklin [35], we artificially fixed the barchan dune by increasing considerably the density of grains at some point after $t = 2.5t_c$. This procedure is similar to that of Ref. [35], where the fluid flow was reduced after $t = 2.5t_c$ in order to remain slightly below the threshold for bed load. Neglecting bed load in the subaqueous case is justified by its smaller effect on the water (feedback effect) when compared with the shape perturbation [35,45]. We adopted the same coordinate system as in Ref. [35], with the origin of the longitudinal coordinate at the dune crest, as shown in Fig. 6, and the use of the displaced coordinate $y_d = y - h(x)$, where $h(x)$ is the local height of the barchan in its vertical symmetry plane.

Figures 7 and 8 show the second-order moments for the flow over the barchan dune. Figures 7(a), 7(b), and 8 present some profiles of $\overline{u'u'}$, $\overline{v'v'}$, and $-\overline{u'v'}$, respectively, for different longitudinal positions. In these figures, the abscissa corresponds to $\overline{u'u'}$, $\overline{v'v'}$, or $-\overline{u'v'}$ normalized by u_*^2, the ordinate to the displaced coordinate y_d normalized by δ, and each different symbol to the longitudinal position normalized by L with the origin at the dune crest. The plotted positions are listed in the key of Fig. 7(a).

The profiles of Figs. 7 and 8 are very much like Figs. 16 and 17(b) of Ref. [35]. In particular, we note that the
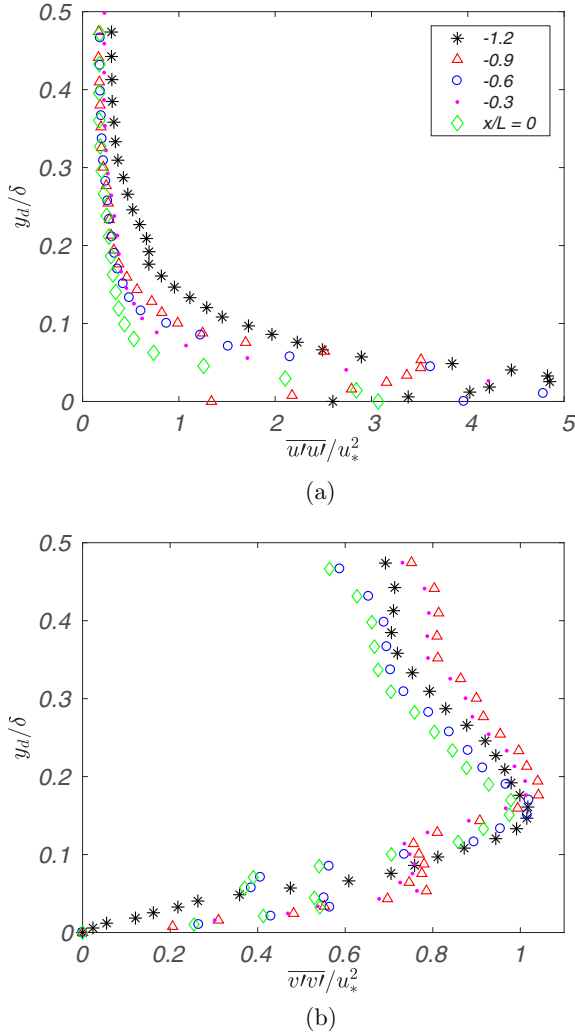
(a)

(b)

FIG. 7. Profiles of (a) $\overline{u'u'}$ and (b) $\overline{v'v'}$ normalized by u_*^2, using the displaced coordinate y_d normalized by δ. Each different symbol corresponds to a longitudinal position normalized by L, with the origin at the dune crest, and listed in the key.

maximum value of $-\overline{u'v'}$ is attained within $-1.2 < x/L < -0.6$, reaching values of approximately $1.1u_*^2$, just as measured experimentally. In summary, the evolution of second-order moments along the dune obtained from our LES simulations is in good agreement with the results of Ref. [35], showing that the numerical setup adopted captures the mean features associated with the turbulent flow over the dune.

3. Trajectories of grains

In Ref. [13], we presented the trajectories of grains migrating to the horns of barchans during their growth from conical piles that consisted of $0.40 \leqslant d \leqslant 0.60$ mm glass beads. We present next the trajectories of grains that migrated to the growing horns of barchans obtained from numerical simulations. In the simulations, we tracked only grains moving over the dune (over a granular bed), because grains moving directly over the channel wall presented straighter trajectories when compared with experiments. This difference may be connected to the microstructure of the grain and wall surfaces,
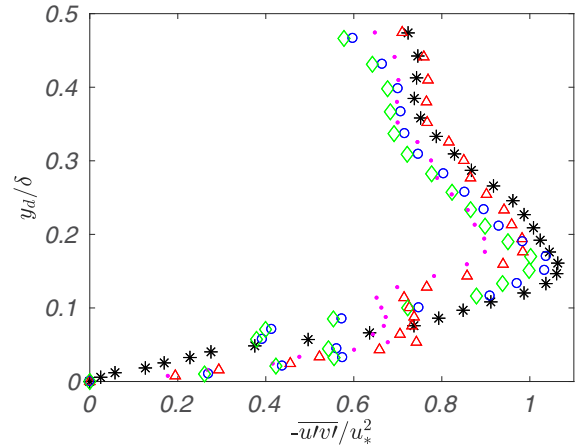

FIG. 8. Profiles of $-\overline{u'v'}$ normalized by u_*^2, using the displaced coordinate y_d normalized by δ. Each different symbol corresponds to a longitudinal position normalized by L, with the origin at the dune crest, and listed in the key of Fig. 7(a).

which are smoother in the numerical simulations, and, therefore, affect strongly grains rolling and sliding directly over the bottom wall. In the experiments of Ref. [13], we expect that the channel wall was subject to small scratches caused by the grains in addition to other sources of microstructure uncertainties.

Figure 9 shows the pathlines of some grains that migrated to horns during the growth of a barchan dune from an initially conical pile for the numerical simulations with $Re = 1.82 \times 10^4$. The abscissa and ordinate correspond, respectively, to the transverse and streamwise coordinates, z and x, normalized by R. In Fig. 9, the dashed black circle displays the initial pile. We observe a behavior similar to that noted in Ref. [13], with grains that migrate to horns describing circular paths, which implies significant transverse components. As verified experimentally by Ref. [13], these grains come from regions upstream of the dune centroid, moving around the central region of the barchan before reaching the horns.
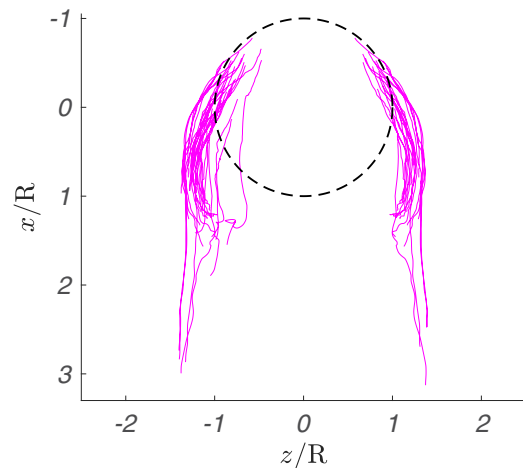

FIG. 9. Trajectories of some of the grains that migrated to horns during the growth of a barchan dune. The water flow is from top to bottom. $Re = 1.82 \times 10^4$, and the dashed black circle represents the initial pile of radius R.
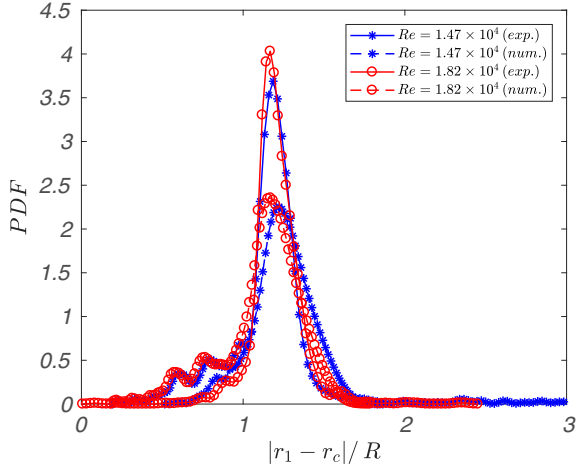
FIG. 10. PDFs of the original positions of the grains that migrated to horns during the growth of a barchan dune, obtained from numerical simulations and the experiments of Ref. [13]. A kernel smoothing function was used in these plots [48].

Alvarez and Franklin [13] used radial and angular coordinates with the origin at the dune centroid in order to find the original positions of grains migrating to the growing horns, and afterward they computed their probability density functions (PDFs) and frequencies of occurrence. We make use here of the same method, in which we localize in polar coordinates the grains migrating to horns. The polar coordinates were defined as $(|r_1 - r_c|, \phi)$, in the same way as in Ref. [13], r_1 being the original position of grains, r_c the instantaneous position of the dune centroid, and ϕ the angle with respect to the transverse direction.

Figures 10 and 11 present the PDFs of the initial positions of grains migrating to horns as functions of $|r_1 - r_c|/R$ and their frequencies of occurrence as functions of ϕ, respectively, for both our numerical results and the experiments of Ref. [13]. The PDFs of Fig. 10 were computed using a kernel smoothing function [48] and the water flow direction in Fig. 11 is 270°. Figures 10 and 11 show a good agreement between experiments and numerical simulations, most of the
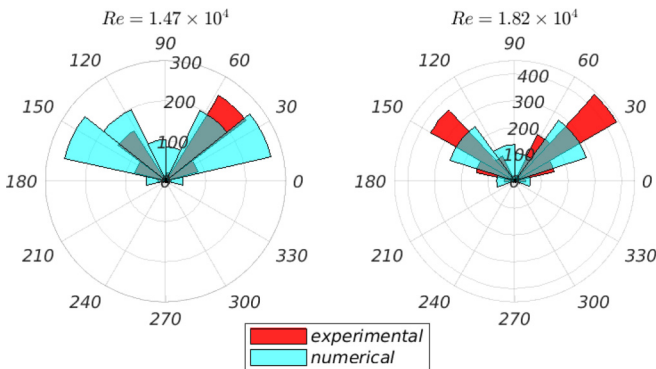

FIG. 11. Frequencies of occurrence of the initial positions of grains migrating to horns as functions of the angle with respect to the transverse direction (water flow direction is 270°), obtained from numerical simulations and the experiments of Ref. [13]. The tips of appearing horns point to angles of approximately 240° and 300°.
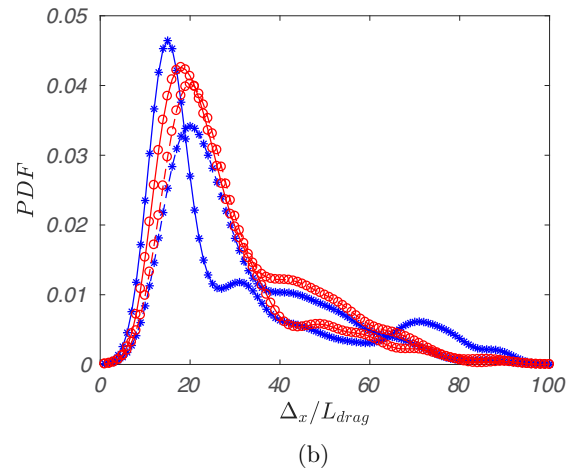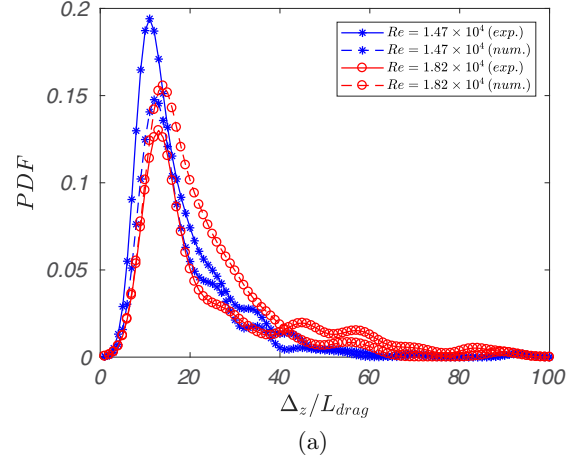

FIG. 12. PDFs of the total (a) transverse and (b) longitudinal distances, Δ_z and Δ_x, normalized by L_{drag} for numerical and experimental results, as listed in the key of part (a).

grains that migrate to horns being originally within $|r_1 - r_c|/R > 1$ and $15° \leqslant \phi \leqslant 70°$ and $120° \leqslant \phi \leqslant 170°$, i.e., at upstream regions on the periphery of the pile.

We computed the total transverse (Δ_z) and longitudinal (Δ_x) distances traveled by the grains that migrated to horns. Figures 12(a) and 12(b) present PDFs of Δ_z/L_{drag} and Δ_x/L_{drag}, respectively, obtained from both the present simulations and the experiments of Ref. [13], and the cases are listed in the key of Fig. 12(a). For both the numerical simulations and experiments, we observe a significant transverse component in the movement of grains, corroborating the conclusion of Ref. [13] that in the subaqueous case grains migrating to horns describe circular paths with important transverse components. By considering the most probable values of the distributions, we find $11 \leqslant \Delta_z/L_{\text{drag}} \leqslant 13$ and $\Delta_z/\Delta_x \approx 0.5$ for the simulations, close to the values $10 \leqslant \Delta_z/L_{\text{drag}} \leqslant 12$ and $\Delta_z/\Delta_x \approx 0.5$ found for the experiments.

4. Granular flux

We present next the flux of grains along the subaqueous barchan, which still needs investigation even experimentally. For that, we computed the total number of grains crossing certain barchan cross sections (x planes) during specific
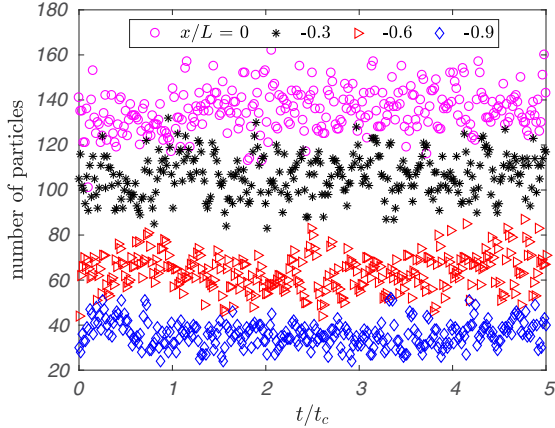
FIG. 13. Number of grains crossing certain barchan cross sections as a function of the normalized time t/t_c. The longitudinal positions of each considered cross section (x planes) are listed in the figure key (and shown in Fig. 6), and Re $= 1.47 \times 10^4$. For these computations, a time interval of 0.13 s was used.

periods. By using relatively short periods, we obtained *quasi-instantaneous* values for the flux.

Figure 13 presents the number of grains crossing certain barchan cross sections as a function of the normalized time t/t_c, where an interval of 0.13 s was used in the computations, corresponding to $0.016t_c$. Values presented in the ordinate can be converted to g by multiplying them by 1.64×10^{-4}, which corresponds to the grain mass in g. In spite of considerable dispersion, Fig. 13 shows that, locally, there seems to exist a transient in the flux of grains for $t/t_c \lesssim 1.5$ and afterward the flux is roughly constant. This is, in some measure, consistent with the characteristic time $t/t_c = 2.5$ for the growth of barchans proposed by Ref. [12]. In space, Fig. 13 shows that the flux is not saturated along the barchan, increasing toward the crest. Although it is known that the largest value should occur just upstream of the dune crest [49], we are not able to
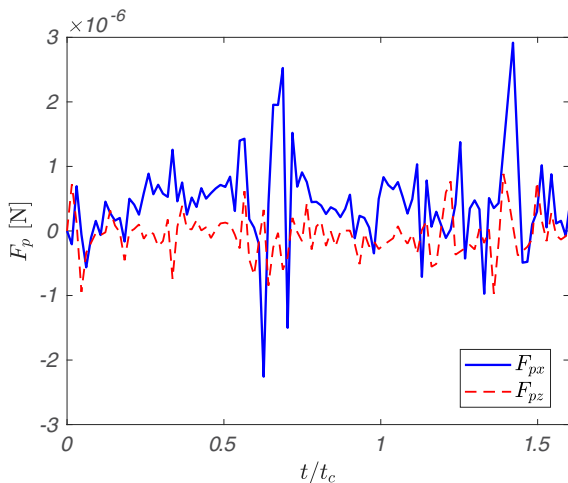
show that for the moment given the relatively high dispersion in obtained fluxes.

5. *Forces on grains*

The present simulations provide us with the resultant force acting on each grain, $\vec{F}_p$, corresponding to the right-hand side of Eq. (1), i.e., $\vec{F}_p = \vec{F}_{fp} + \vec{F}_c + m_p\vec{g}$. This information is difficult to access experimentally, and it is not available from current experiments. In this section, we analyze the resultant force on grains along the barchan dune.

Figure 14 presents the resultant force on a tracked grain as it was entrained from an upstream region until the dune crest, and it is representative of the resultant force acting on grains migrating toward the crest. In Fig. 14, the solid blue line corresponds to the longitudinal component of the force, F_{px}, and the dashed red line to the transverse component of the force, F_{pz}. We observe that the grain experiences a varying force, in the transverse direction the instantaneous values varying around a zero average, while in the longitudinal
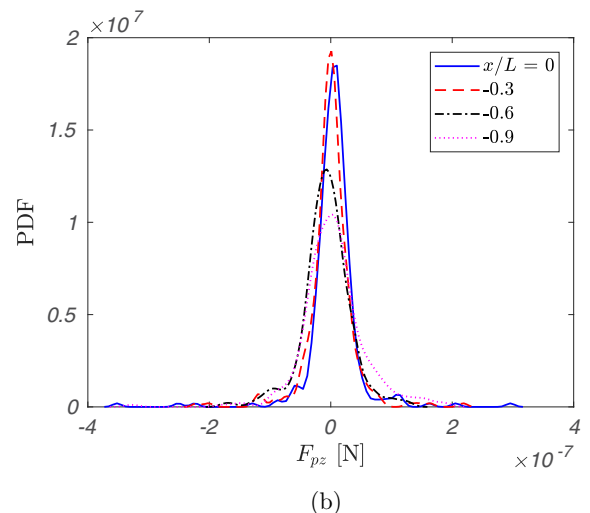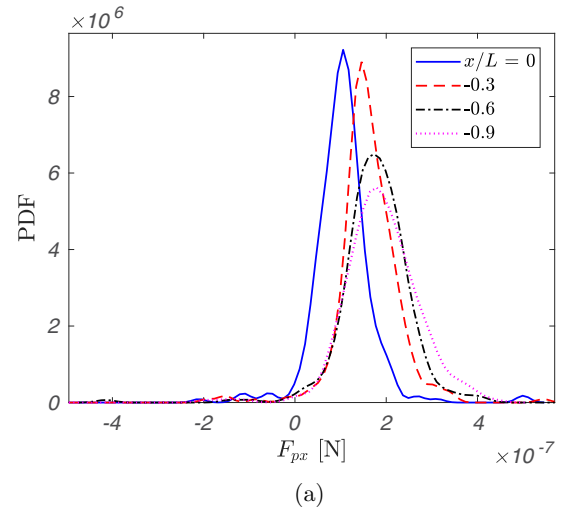

(a)

(b)

FIG. 15. PDFs of (a) longitudinal and (b) transverse components of the resultant force acting on each grain crossing a given barchan cross section. The longitudinal positions of each considered cross section (x planes) are listed in the figure key and Re $= 1.47 \times 10^4$.

FIG. 14. Longitudinal and transverse components of the resultant force on a grain, F_{px} and F_{pz}, respectively, as a function of time. This specific grain was entrained from an upstream region toward the crest, and Re $= 1.47 \times 10^4$.

direction the force has a positive average, with high peaks occurring in some occasions. These peaks are much higher than the mean value (in Fig. 14, the highest peak is one order of magnitude greater than the mean value). It is interesting to note that this specific grain took slightly longer than $1.5t_c$ to reach the dune crest, with the highest peak occurring just before reaching the crest.

Figures 15(a) and 15(b) present, respectively, PDFs of the longitudinal and transverse components of the resultant force acting on each grain crossing a given barchan cross section. Figure 15 shows that the resultant force acting on each grain has a longitudinal component that attains higher values on upstream regions and decays toward the crest, with a slightly broader distribution upstream, while the transverse component is always peaked at zero, also with a broader distribution upstream. Although the longitudinal component of the resultant force is lower at the crest, the granular flux increases toward the crest, as shown in Sec. IV B 4, due probably to the grain inertia. We expect that at the crest the granular flux is lower than that just upstream of it, but, as explained in Sec. IV B 4, the relatively high dispersion in computed fluxes does not allow us to prove that for the moment.

The results on the resultant force, which have until now been only conjectured, help to explain the mechanism of upstream erosion and crest deposition that exists on barchan dunes.

V. CONCLUSIONS

This paper investigated numerically the formation and evolution of single barchans by using the computational fluid dynamics–discrete element method (CFD-DEM), where the DEM was coupled with the large eddy simulation (LES). Our simulations reproduced numerically the experiments of Alvarez and Franklin [12,13], performed in a closed-conduit channel where initially conical heaps evolved to single barchans under the action of a turbulent water flow. The numerical setup used the same initial and boundary conditions of the experiments of Refs. [12,13].

Our simulations captured well the evolution of the initial pile toward a barchan dune in both the bedform and grain scales. Concerning the bedform, the morphology obtained from our numerical simulations showed the same characteristic time and length observed in experiments: the horns grow and the dune width and length evolve until $t = 2.5t_c$, where t_c is a timescale proposed in Ref. [12], reaching a stable value for $t > 2.5t_c$. The evolution of the horn length, its final value, and that of the dune width and length are in excellent agreement with the experiments of Refs. [12,13].

The water flow over a fixed barchan was compared with similar experiments reported in Charru and Franklin [35]. The evolution of second-order moments along the dune obtained from our LES simulations is in good agreement with the results of Ref. [35], showing that the numerical setup adopted is able to capture the mean features associated with the turbulent flow over the dune.

We tracked the grains that migrated to the growing horns of barchans. We observed a behavior similar to that observed in Ref. [13], with grains that migrate to horns describing circular paths. Plots in polar coordinates centered at the dune centroid showed that these grains come from upstream regions on the periphery of the initial pile. In addition, computations of the total transverse and longitudinal distances traveled by the grains showed PDFs similar to experimental values and a ratio between the transverse and longitudinal distances of approximately 0.5, the same value obtained experimentally.

Finally, we obtained the local granular flux and the resultant force acting on each grain, the latter not yet previously measured nor computed. Concerning the granular flux, we showed that there exists a transient for $t/t_c \lesssim 1.5$ and that it is not saturated along the barchan. For the resultant force on each grain, we showed that its longitudinal component attains higher values on upstream regions and decays toward the crest. These results help to explain the mechanism of upstream erosion and crest deposition that exists on barchan dunes.

The good agreement between the numerical and experimental results shows that the present method is appropriate for numerical computations of bedforms, opening new possibilities for accessing data not available from current experiments, such as, for example, the instantaneous forces on each grain within the bed.

[1] R. A. Bagnold, *The Physics of Blown Sand and Desert Dunes* (Chapman and Hall, London, 1941).

[2] P. Hersen, S. Douady, and B. Andreotti, Phys. Rev. Lett. **89**, 264301 (2002).

[3] P. Claudin and B. Andreotti, Earth Planet. Sci. Lett. **252**, 20 (2006).

[4] E. J. R. Parteli and H. J. Herrmann, Phys. Rev. E **76**, 041307 (2007).

[5] E. M. Franklin and F. Charru, Powder Technol. **190**, 247 (2009).

[6] E. M. Franklin and F. Charru, J. Fluid Mech. **675**, 199 (2011).

[7] M. R. M. Penteado and E. M. Franklin, Exp. Therm. Fluid Sci. **78**, 220 (2016).

[8] R. A. Bagnold, Philos. Trans. R. Soc. London, Ser. A **249**, 235 (1956).

[9] R. A. Bagnold, Proc. R. Soc. London A **332**, 473 (1973).

[10] N. Endo, H. Kubo, and T. Sunamura, Earth Surf. Proc. Landforms **29**, 31 (2004).

[11] N. Hori, A. Yamada, Y. Oshiro, and O. Sano, J. Phys. Soc. Jpn. **76**, 024401 (2007).

[12] C. A. Alvarez and E. M. Franklin, Phys. Rev. E **96**, 062906 (2017).

[13] C. A. Alvarez and E. M. Franklin, Phys. Rev. Lett. **121**, 164503 (2018).

[14] J. L. Wenzel and E. M. Franklin, Granular Matter **21**, 321 (2019).

[15] C. A. Alvarez and E. M. Franklin, Phys. Rev. E **100**, 042904 (2019).

[16] G. Sauermann, K. Kroy, and H. J. Herrmann, Phys. Rev. E **64**, 031305 (2001).

[17] H. J. Herrmann and G. Sauermann, Physica A **283**, 24 (2000).

[18] K. Kroy, G. Sauermann, and H. J. Herrmann, Phys. Rev. E **66**, 031302 (2002).

[19] K. Kroy, G. Sauermann, and H. J. Herrmann, Phys. Rev. Lett. **88**, 054301 (2002).

[20] K. Kroy, S. Fischer, and B. Obermayer, J. Phys.: Condens. Matter **17**, S1229 (2005).

[21] V. Schwämmle and H. J. Herrmann, Eur. Phys. J. E **16**, 57 (2005).

[22] E. J. R. Parteli, O. Durán, M. C. Bourke, H. Tsoar, T. Pöschel, and H. Herrmann, Aeol. Res. **12**, 121 (2014).

[23] A. Khosronejad and F. Sotiropoulos, J. Fluid Mech. **815**, 117 (2017).

[24] M. W. Schmeeckle, J. Geophys. Res. Earth Surf. **119**, 1240 (2014).

[25] A. G. Kidanemariam and M. Uhlmann, Int. J. Multiphase Flow **67**, 174 (2014).

[26] D. Liu, X. Liu, X. Fu, and G. Wang, J. Geophys. Res. Earth Surf. **121**, 767 (2016).

[27] R. Sun and H. Xiao, Comput. Geosci. **89**, 307 (2016).

[28] T. Pähtz and O. Durán, Phys. Rev. Fluids **2**, 074303 (2017).

[29] A. G. Kidanemariam and M. Uhlmann, J. Fluid Mech. **750**, R2 (2014).

[30] A. G. Kidanemariam and M. Uhlmann, J. Fluid Mech. **818**, 716 (2017).

[31] C. Goniva, C. Kloss, N. G. Deen, J. A. M. Kuipers, and S. Pirker, Particuology **10**, 582 (2012).

[32] C. Kloss and C. Goniva, in *Proceedings of the Fifth International Conference on Discrete Element Methods* (2010).

[33] R. Berger, C. Kloss, A. Kohlmeyer, and S. Pirker, Powder Technol. **278**, 234 (2015).

[34] M. Colombini, J. Fluid Mech. **756**, 1 (2014).

[35] F. Charru and E. M. Franklin, J. Fluid Mech. **694**, 131 (2012).

[36] P. A. Cundall and O. D. Strack, Géotechnique **29**, 47 (1979).

[37] Y. Tsuji, T. Tanaka, and T. Ishida, Powder Technol. **71**, 239 (1992).

[38] Y. Tsuji, T. Kawaguchi, and T. Tanaka, Powder Technol. **77**, 79 (1993).

[39] Z. Y. Zhou, S. B. Kuang, K. W. Chu, and A. B. Yu, J. Fluid Mech. **661**, 482 (2010).

[40] F. Nicoud and F. Ducros, Flow Turbul. Combust. **62**, 183 (1999).

[41] D. Gidaspow, *Multiphase Flow and Fluidization: Continuum and Kinetic Theory Descriptions* (Academic, San Diego, California, 1994).

[42] D. H. Kelley and N. T. Ouellette, Am. J. Phys. **79**, 267 (2011).

[43] C. A. Alvarez and E. M. Franklin, Physica A **465**, 725 (2017).

[44] R. D. Moser, J. Kim, and N. N. Mansour, Phys. Fluids **11**, 943 (1999).

[45] E. M. Franklin, F. T. Figueiredo, and E. S. Rosa, J. Braz. Soc. Mech. Sci. Eng. **36**, 725 (2014).

[46] F. D. Cúñez, G. V. G. Oliveira, and E. M. Franklin, J. Braz. Soc. Mech. Sci. Eng. **40**, 138 (2018).

[47] See Supplemental Material at http://link.aps.org/supplemental/10.1103/PhysRevE.101.012905 for a movie from our numerical simulations showing the growth of a barchan dune.

[48] A. Bowman and A. Azzalini, *Applied Smoothing Techniques for Data Analysis* (Oxford University Press, Oxford, 1997).

[49] F. Engelund and J. Fredsoe, Annu. Rev. Fluid Mech. **14**, 13 (1982).